This is a preprint, the final version is subject to change, of the American Mineralogist (MSA)
Cite as Authors (Year) Title. American Mineralogist, in press.
(DOI will not work until issue is live.) DOI: http://dx.doi.org/10.2138/am-2017-6093

Revision 1

A new hydrothermal moissanite cell apparatus for optical in-situ observations at high pressure and high temperature, with applications to bubble nucleation in silicate melts

Matteo Masotta and Hans Keppler[2]

[1]*Dipartimento di Scienze della Terra, Università di Pisa - Via S. Maria 53, 56126 Pisa, Italy*
[2]*Bayerisches Geoinstitut, Universität Bayreuth, D-95440 Bayreuth, Germany*

Abstract

We present a new hydrothermal moissanite cell for in-situ experiments at pressures up to 1000 bar and temperature to 850 °C. The original moissanite cell presented by Schiavi et al. [*Am. Mineral. 95, 2010*] was redesigned to allow precise control of fluid pressure. The new device consists of a cylindrical sample chamber drilled into a bulk piece of NIMONIC 105 super alloy, which is connected through a capillary to an external pressure control system. Sealing is provided by two gold gasket rings between the moissanite windows and the sample chamber. The new technique allows the direct observation of various phenomena, such as bubble nucleation, bubble growth, crystal growth, and crystal dissolution in silicate melts, at accurately controlled rates of heating, cooling and compression or decompression.

Several pilot experiments on bubble nucleation and growth at temperature of 715 °C and under variable pressure regimes (pressure oscillations between 500 and 1000 bar and decompression from 800 to 200 bar at variable decompression rates) were conducted using a haplogranitic glass as starting material. Bubble nucleation occurs in a short single event upon heating of the melt above the glass transition temperature and upon decompression, but only during the first 100 bar of decompression. New bubbles nucleate only at a distance from existing bubbles larger than the mean diffusive path of water in the melt. Bubbles expand and shrink instantaneously in response to any pressure change. The bubble-bubble contact induced during pressure cycling and decompression does not favor bubble coalescence, which is never observed at contact times shorter than 60 s. However, repeated pressure changes favor the diffusive coarsening of larger bubbles at the expense of the smaller ones (Ostwald ripening). Experiments with the haplogranite show that, under the most favorable conditions of volatile supersaturation (as imposed by the experiment), highly viscous melts are likely to maintain the packing of bubbles for longer time before fragmentation. In situ observation with the new hydrothermal moissanite cell allow to carefully assess the conditions of bubble nucleation, eliminating the uncertainty given by the post mortem observation of samples run using conventional experimental techniques.

Keywords: moissanite cell, in-situ observation, bubble nucleation, bubble coalescence, degassing, decompression, Ostwald ripening

Introduction

Magmatic degassing controls the intensity and the style of volcanic eruptions. Understanding the mechanisms and rates at which volatiles are exsolved and released from the magma is fundamental for the interpretation of the volcanic activity and the definition of the hazard associated with explosive eruptions. Upon magma ascent, degassing is regulated by bubble nucleation and growth, which occur in response to changes in pressure and temperature. For this reason, bubble nucleation and growth have been the object of experimental investigations over a wide regime of T-P conditions, including isobaric and decompression experiments (Mourtada-Bennefoi and Laporte, 1999; Lensky et al., 2004; Gardner, 2007; Gardner and Ketcham, 2011; Preuss et al., 2016). These studies explored the effect of the physical and chemical properties of the melt (water content, surface tension, viscosity) on the vesiculation process, based on the textural analysis of quenched experiments. The post-mortem analysis of experimental samples is useful to investigate how the final state of a sample changes as a function of the physical conditions simulated during the experiment. Nevertheless, it precludes the evaluation of the early stage of vesiculation or possible effects due to the interaction between the sample and the capsule (e.g., Mangan and Sisson, 2000). The recent development of in-situ experimental techniques (Gondé et al. 2006; Schiavi et al., 2010) improved the understanding of bubble nucleation and growth in silicate melts (Martel and Bureau, 2001; Gondé et al. 2011; Masotta et al., 2014), and helped to validate theoretical models (Fiege and Cichy, 2015; Ryan et al., 2015).

The moissanite cell is a recently developed tool that allows in situ experiments at temperature up to 1250 °C (Schiavi et al., 2010). Compared to other in-situ techniques, such as the hydrothermal diamond anvil cell and modified internally heated autoclaves (e.g., Martel and Bureau, 2001, Gondé et al. 2006; Gondé et al. 2011), the moissanite cell allows high-resolution observations of relatively large samples (several mm in size), with a simple device fitting onto a microscope stage. This technique was used for the in-situ observation of bubble nucleation and growth in basalt, andesite and rhyodacite melt at temperature up to 1240 °C (Masotta et al., 2014), as well as for studying the crystallization of basalt and andesite melt (Ni et al., 2014). The major limitation of this technique is given by the fact that experiments are performed at 1 bar, which prevents the investigation bubble nucleation and growth at realistic T-P conditions. In order to overcome this major limitation, we have modified the setup of the original moissanite cell presented in Schiavi et al. (2010) and designed new components that allow using the cell for experiments at precisely controlled hydrostatic pressures up to at least 1000 bar and at temperatures up to 850 °C. In this paper, we describe the new hydrothermal moissanite cell and illustrate its applications to the in-situ study of bubble growth in a haplogranitic melt. The new cell can reproduce the range of temperature and pressure conditions typical for shallow silicic magma chambers and volcanic conduits, allowing to simulate pre-eruptive processes such as stepped-path or continuous decompression, as well as pressure oscillations due to the passage of seismic waves or magma wagging.

The new hydrothermal moissanite cell

The new hydrothermal moissanite cell resembles the Bassett-type externally heated diamond anvil cell and represents an evolution and re-design of the original moissanite cell presented by Schiavi et al. (2010). Construction diagrams and pictures of the hydrothermal cell are shown in Figure 1; more details are given in the supplementary material. The central part of the cell is made of a single piece of the NIMONIC 105 super alloy. This piece contains a 3.5 mm diameter and 4.0 mm tall

cylindrical sample chamber connected through a ca. 100 μm diameter capillary to the external pressure line. To make this part, a capillary hole was first spark-eroded into a block of the super alloy. Then the hole for the sample chamber was drilled into the piece, such that it intersected the capillary and subsequently, the piece was machined to produce the desired external shape. The sample chamber in the NIMONIC piece is sandwiched between two moissanite anvils (5 x 5 mm cylinders of synthetic gem-quality SiC). Two rings of 150 μm think gold foil, placed between the moissanite and the sample chamber, prevent the fluid from leaking out of the chamber. The moissanite crystals are seated on Inconel plates and rings, which sustain the fluid pressure inside the sample chamber and prevent the outer pyrophyllite parts supporting the heater from breaking during the experiment. Each heater is composed of four shells of fired pyrophyllite surrounding the moissanite crystals and supporting three Pt_{90}-Rh_{10} heating wires (300 μm thick), wrapped in parallel into five coils around the three inner shells. The seats below the moissanite windows are supported by two stainless-steel backing plates, which are compressed by tightening three screws, as in a normal diamond cell. Two independent S-type thermocouples are placed above each heater and cemented on the side of the moissanite crystal. The temperature inside the sample chamber was calibrated against the temperature measured with the two thermocouples attached to the moissanite crystals, using an external thermocouple inserted through a hole drilled in the upper moissanite crystal. The difference between external and internal temperature slightly decreases at increasing temperature, being approximately 35 °C between 600 and 850 °C.

Experimental temperature is controlled by an external control unit, which allows programming variable heating and cooling rates. The maximum temperature at which the cell was tested is 850 °C, at this temperature the heaters require about 13 Amperes and 7 Volts. To reduce heat loss, zirconia polycrystalline fibers (ZrO_2) are placed on top of the heaters and around the sample chamber.

The new hydrothermal moissanite cell can in principle be used together with any pumping system for water or argon. In the experiments described here, the cell was connected with a capillary to a pressure generating system using distilled water as pressure medium. The system consisted essentially of a spindle press (model 750.6201 of SITEC, Switzerland) driven by a step-motor and controlled by an external computer program. Pressure was measured by a wire-strain gauge. We tested the new moissanite cell up to 1000 bar and 850 ˚C. However, the design of the cell should allow reaching pressures of at least 2000 bar.

Experimental methods

Starting material

Hydrous glass samples were prepared in the form of disks of 3 mm diameter and 100 μm thickness, polished on both sides. The sample disk was sandwiched between two quartz cylinders that prevent the sample from moving or deforming upon compression and decompression of the fluid inside the sample chamber. The experiments were performed using a haplogranite glass as a starting material with an anhydrous base composition $Ab_{40}Qz_{35}Kfs_{25}$ (the same starting material as in Masotta and Keppler, 2015). The haplogranitic composition offers the advantages of a relatively low melting temperature (T_{liq} < 800 °C in water-bearing systems) and physical properties not far from those of natural rhyolites. The haplogranitic glass was synthesized in a chamber furnace at 1600 °C, then crushed into powder and re-melted in the presence of excess water in a 3.5 mm diameter gold

capsule at 1000 bar and 1000 °C for 5 days in a TZM vessel. The re-melting at high pressure also removes air bubbles trapped during the synthesis of the glass in the chamber furnace that may affect bubble nucleation kinetics during the experiment at high pressure (Preuss et al., 2016). Sample capsules were sliced and polished on both sides, to form 100 μm-diameter disks that were eventually used as samples for experiments in the hydrothermal moissanite cell. Some samples were run without removing the gold capsule ring, in order to check the effect of sample deformation during melting. No differences were observed between samples run with the gold capsule ring and samples run without. FTIR and microprobe analyses of the starting glasses yielded a composition of 3.66 wt.% H_2O, 6.34 wt.% Na_2O, 6.02 wt.% K_2O, 16.95 wt.% Al_2O_3, and 70.69 wt.% SiO_2. Water contents were quantified using the infrared extinction coefficients for water in rhyolite glass by Withers and Behrens (1999).

High pressure experiments

After the preparation of the heaters, the two halves of the cell were pre-heated separately for few hours at about 600 °C, in order to dry the cement supporting the pyrophyllite parts. After this procedure, the cell was assembled for the experiment. The glass disk sample was sandwiched between two quartz cylinders and loaded in the sample chamber. The sample chamber was then inserted between the two halves of the moissanite cell, with the gold gaskets centered on the moissanite crystals. The cell was then closed by tightening the three screws connecting the two halves, filled with zirconia fibers, connected with the heating and pressure control systems and placed under the optical microscope.

Before heating, the cell was pressurized with a rate of 100-500 bar/min and pressure was held for a few minutes to check for leaking. After this step, temperature is increased to about 450 °C and held at this temperature for about one hour, in order to warm up the metal parts before the final heating and to check for leaking at high temperature. Temperature was then increased with heating rates up to 167 °C/min and held constant at the set point (750 °C) for the duration of the experiment. It should be noted that, based on the temperature calibration run, the actual heating rate inside the sample chamber is approximately half of the heating rate measured at the thermocouple and that in thermal equilibrium, the internal temperature is about 35 °C lower. At the end of the experiment, temperature and then pressure were decreased, the cell was opened and the sample extracted from the sample chamber for post-mortem analysis.

Image acquisition and analysis

A digital camera placed on a transmission optical microscope (Zeiss Axioscope 40; output to either eyepieces or camera-computer) recorded time-lapse pictures and movies of the sample. Image analysis of bubbles was carried out using the free WEB software package ImageJ (Image Processing and Analysis in Java; http://rsb.info.nih.gov/ij/). Microscope pictures were converted to binary (8 bit) images. To limit the error on particle counting and measuring, the touching edges of adjacent bubbles were drawn manually.

Experimental results

To demonstrate the capabilities of the new hydrothermal moissanite cell, we describe here a series of pilot experiments carried out at pressures between 200 and 800 bar and at an external

temperature of 750 °C (i.e. a sample temperature of 715 °C). These experiments investigated bubble growth in the haplogranitic melt at both isobaric conditions, during pressure oscillations, and at different decompression rates, and produced overall consistent results. Details of the experiments are compiled in Tables 1 and 2. The P-t path of a typical experiment (HGT-2) is shown in Figure 2. After the initial heating to the external set point temperature of 750 °C (time 0:00), the temperature remained constant during the entire experiment. Several videos of this experiment are also available online as supplementary material. In the following sections, we will discuss the main observations during this experiment in detail.

Initial bubble nucleation

Bubble nucleation in the haplogranite occurred nearly instantaneously upon heating of the sample, when the temperature crossed 550 °C, which likely corresponds to the glass transition temperature. The driving force for the bubble nucleation is the initial oversaturation of the glass with water. The synthesis conditions of the glass should yield an equilibrium water content near 4 wt. %, consistent with the 3.66 wt. % measured by FTIR, while at 600 bar and 750 °C, a water solubility near 3 wt. % is expected (Holtz et al., 1995). At 550 °C, the melt became darker for few seconds, due to sudden nucleation of bubbles, then bright again after reaching 700 °C. Experiments performed with basalt and andesite in the standard moissanite cell at 1 bar (Masotta et al., 2014) showed a complete darkening of the glass during the heating, due to the formation of crystal nuclei that acted as preferential nucleation surfaces by reducing the supersaturation pressure (ΔP). Compared to these melts, the haplogranite is unlikely to have nucleated crystals during heating, but rather, bubbles nucleated homogeneously in the melt (see discussion below). Here and in the following discussion, we will always assume that the glass/melt disc essentially behaved like a chemically closed system. This is justified by the sample geometry with the thin disc being sandwiched between two quartz discs. Upon crossing the glass transition temperature, a tight contact of the melt with both quartz discs was established, such that the water used as pressure medium could only interact with the outer cylindrical surface of the 3 mm diameter sample disc. This diameter is much larger than the free diffusion path of water in the melt during the duration of the experiment (about 0.3 mm for 1 hour at 715 °C; Nowak and Behrens 1997). However, since the melt contained abundant bubbles of water vapor after the first nucleation event, it likely remained in a state close to vapor saturation throughout the entire experiment.

Bubble growth and number density at isobaric conditions

Bubble growth rate (G_R) was determined under isobaric-isothermal conditions (600 bar, 715 °C), before and after several cycles of pressure oscillations (see Figure 2). Growth rate was measured on several bubbles of different size, measuring the difference in bubble radius over elapsed time (mm/s). Bubble growth was largest shortly after nucleation and decreased rapidly with time, with G_R being $5(\pm1)\cdot10^{-6}$ mm/s after the first 10 minutes and $2(\pm1)\cdot10^{-7}$ mm/s over the subsequent 3 hours of the experiment (Table 3). This observation is consistent with the logarithmic decay of bubble growth inferred from previous in situ experiments performed with other SiO_2-rich melt compositions, such as haplogranite (G_R is $4.5\cdot10^{-4}$ mm/s in the first 10 seconds; Gondé et al., 2011) and rhyodacite (G_R is $7.1\cdot10^{-6}$ mm/s in the first 8 minutes; Masotta et al., 2014).

Diffusive growth was the principal long-term mechanism of bubble growth, with bubble coalescence being noticeable at the early stage of the experiment and over longer time at constant pressure. Ostwald ripening was also observed, particularly in the isobaric stage that followed the

pressure perturbation, as indicated by the negative growth of smaller bubbles and their complete dissolution in the melt during the 1.5-hour isobaric dwell (Figure 3). The combined effect of coalescence and Ostwald ripening that followed the cycle of pressure perturbations resulted in an overall decrease of the bubble number density (N_B), according to a power law (Figure 4a; Table 3). Apparently, pressure perturbations had no effect on the bubble size distribution (BSD), which remained nearly unimodal over time (Figure 4b). In the same way, the cumulative BSD curve maintained the exponential decrease (Figure 4c).

Bubble nucleation and growth during pressure cycle

A sequence of sinusoidal pressure cycles with different periods and amplitudes was imposed on the sample at isothermal conditions (715 °C). Here we discuss the effects of 200 bar amplitude sinusoidal oscillations, over an initial pressure of 600 bar, with periods of 120 and 30 seconds (Figure 2b). Bubbles responded instantaneously to the change of pressure, by shrinking when pressure increased and expanding when pressure decreased. Bubble nucleation always occurred in the larger portions of melt, at half of the distance between the two nearest bubbles, with the average distance being usually 10-30 μm. The N_B changed during the pressure cycle, decreasing in the high-pressure stage, due to the complete dissolution of smaller bubbles, and increasing during the decompression, due to nucleation of new bubbles as result of the increasing supersaturation. However, no major change of N_B and BSD was observed at the end of the last cycle (8 cycles with 120 s period, 15 cycles with 30 s period). This can be observed in the sequence of images in Figure 5, showing pictures taken at the same pressure but after several pressure cycles with roughly the same bubble size, number and distribution. Only by comparing the images collected during the low-pressure phase of the cycle, it is possible to observe a perceptible reduction of the number of small bubbles. As discussed further in the text, this reduction is mostly due to Ostwald ripening and, to a lesser extent, selective coalescence of small bubbles (<10 μm).

Bubble nucleation and growth during decompression

After the pressure cycling and the isobaric dwell, the haplogranite melt was decompressed three times from an initial pressure of 800 bar down to 200 bar, with constant rates of 50, 200 and 400 bar/min. Upon compression to 800 bar, the bubble volume fraction decreased to about 0.15, due to the shrinking of large bubbles and the dissolution of smaller ones. The dissolution of the small bubbles also reduced the N_B. Bubble nucleation started at the onset of decompression and continued for about 2 minutes in the 50 bar/min decompression path, for 1 minute at 200 bar/min and for 30 seconds at 400 bar/min. This means that in all the three decompression runs, nucleation initiated upon decompression near the initial pressure of 800 bar and terminated at about 700 bar. At this pressure, the bubble volume fraction was always about 0.30. No further nucleation occurred after the first 100 bar decompression, but only the expansion of already existing bubbles with the overall increase of the bubble volume fraction. As already observed during the pressure cycles, nucleation occurred in the larger spots of melt at half distance between two nearest bubbles (on average 30 μm; Figure 6a). The nucleation rate increases with the increasing decompression rate, causing at the same time the increase of the N_B and the broadening of the BSD (Figure 6b). The N_B values measured from frames collected at the pressure of 400 bar during the two decompression paths performed at 50 and 400 bar/min, are $2.4 \cdot 10^4$ and $3.2 \cdot 10^4$ mm^{-3}, respectively (Table 3). This is in agreement with experimental results from Gondé et al. (2011), who also found a positive correlation between N_B and decompression rates, and measured similar values of N_B (ranging from 1.0 to

$7.9 \cdot 10^4$ mm^{-3}) in quench samples of haplogranite decompressed to similar final pressures (200-500 bar) with comparable decompression rates (42-252 bar/min).

In each decompression run, the volume fraction of bubbles reached a critical value of about 0.75±0.05 at a pressure slightly above 200 bar, before the melt films between bubbles started to collapse. Just before the fragmentation of the melt (i.e., few seconds after reaching the final pressure of 200 bar), pressure was increased again in order to let the melt recover and start a new decompression path. Only in the last decompression run, pressure was kept at 200 bar to allow full fragmentation. Unfortunately, at this stage, the transparency of the sample decreased, preventing any observation. It was possible, however, to recover the sample after cooling to temperature and to inspect the texture under the electron microscope. The backscattered images show a texture that looks similar to that of highly vesiculated pumices (Figure 7a). Experiment HGT-1 cooled at constant pressure after decompression to 400 bar (Table 2), shows how the texture must have looked like before the fragmentation, except for the presence of tabular feldspars formed during the cooling (Figure 7b).

Discussion

Bubble nucleation at high pressure

An extensive, homogeneous bubble nucleation occurred during the heating at isobaric condition (600 bar) in a short time (few seconds) and was then followed by the rapid growth of bubbles by both diffusive growth and coalescence. Moreover, upon subsequent decompression, bubble nucleation occurred already during the first 100 bar. The supersaturation pressure observed in our experiments is therefore small compared to the ΔP reported in previous studies (e.g., Mourtada-Bonnefoi and Laporte, 2002). As an example, Hurwitz and Navon (1994) performed decompression experiments using a rhyolite and observed homogeneous nucleation of only few bubbles at ΔP between 150 and 700 bar and of a large number of bubbles at ΔP exceeding 800 bar. This discrepancy may be attributed to the difference between in situ observation and post mortem analysis of samples. Experiments by Hurwitz and Navon (1994), as many decompression experiments reported in the literature, were performed using autoclaves equipped with a rapid quench device. During the quench, the drop of the sample in the cold zone of the autoclaves produces an increase of the pressure of several tens of bar. Such an increase in pressure, coupled with the increasing water solubility during cooling of the sample, may have annealed the population of small bubbles, leading to the conclusion that homogeneous nucleation was limited or even not possible at low degrees of supersaturation. However, our in-situ experiments imply that not just nucleation, but also dissolution of bubbles in the melt occurred nearly instantaneously at any time that pressure was increased, as demonstrated by the observation of continuous nucleation and dissolution during the 200 bar amplitude pressure cycling at different periods (Figure 5). This underlines the need of in-situ observations for precise determination of the conditions for bubble nucleation and growth in silicate melt. An alternative explanation for the apparent discrepancy between our results and previous studies could be related to the fact that in our runs, the sample already contained bubbles at the beginning of decompression and therefore had been in a water-saturated state for a long time. Possibly, such melts could contain local clusters or submicroscopic bubbles of water molecules that may act as nucleation/growth sites upon further decompression.

Bubble growth at high pressure

Bubble growth by coalescence occurred at isobaric-isothermal conditions with a constant rate of ~10 $mm^{-3}s^{-1}$, comparable to that of the rhyodacite experiment of Masotta et al. (2014). The rate of coalescence did not change even when pressure oscillations were applied and contact between bubbles was induced by the expansion of the bubbles in the low-pressure stage of the cycles (Figure 5). This means that the relaxation time (τ) required for the coalescence of two bubbles in the haplogranite is longer than the cycle of the pressure perturbations and bubbles are more likely to deform than to coalesce. The cycles with periods of 120 and 30 s yielded a decompression of 200 bar in 60 and 15 s, respectively. The relaxation time (τ), which can be expressed by the relation:

$$\tau = \frac{R\eta}{\sigma}$$

can be calculated for the radius of the bubbles (R), given a shear viscosity (η) of 10^6 Pa·s (Hess and Dingwell, 1996) and a surface tension (σ) of 0.15 N m^{-1} (Bagdassarov et al., 2000). Assuming an average bubble radius of 15 μm, the value obtained is ca. 100 s, which is in excess of the time spent by the bubbles in close contact. The relaxation time decreases with the decreasing size of the bubbles, being lower than 60 s for bubbles smaller than 10 μm. Consistently, the few episodes of coalescence observed during the 120 s pressure cycle are limited to bubbles smaller than this size (Figure 5). The pressure drop occurring during the cycles roughly corresponds to decompression of ~0.33 MPa/s and ~1.33 MPa/s, for the cycles with period of 120 s and 30 s, respectively. Such rates are higher than the decompression rates typical of Plinian eruption (~0.15 MPa/s; Sparks et al., 1994) and the fact that they do not produce a substantial change in the N_B indicates that the ability of bubbles to coalesce is reduced when the decompression rate is fast enough.

One important observation of the bubble evolution during the pressure cycle is the occurrence of Ostwald ripening. In previous experiments with the moissanite cell (Masotta et al., 2014), this process was observed only in the melt with lower viscosity (basalt) and only at later stage of the experiment, when the bubble size distribution was heterogeneous. Normally, in a steady state condition, Ostwald ripening is much slower than other mechanisms of bubble growth, especially for more viscous systems (Yamada et al., 2008). In the experiment, however, the cycles of bubble expansion and resorption imposed by the pressure variations, set the system in a persistently transient regime, due to the longer time required to exsolve/dissolve volatiles in the bubble/melt compared to the time required by the bubble to expand/shrink with changing pressure. Under these conditions, Ostwald ripening is highly favored and the time scale for diffusive coarsening may be significantly reduced. This is consistent with experimental observation by Lautze et al. (2011), as well as with theoretical consideration of Chen and Voorhees (1993). The period of the pressure perturbation seems to inversely correlate with the time scale of the diffusive coarsening, with the longer period cycle yielding lower time scales for diffusive coarsening and a more evident effect of Ostwald ripening. This observation, however, may be influenced by the fact that the effects of the short period cycle are superimposed on those of the long period one, as the cycles were performed in sequence. To resolve the effect of the period on the effectiveness of Ostwald ripening, additional experiments would be required.

Decompression and fragmentation of the melt

The decompression rates used in our experiments range from 50 to 400 bar/min. For this range of decompression rates, Gardner et al. (1999), Mourtada-Bennefoi and Laporte (2004) and Gondé et al. (2011) demonstrated experimentally that the N_B increases with the increasing decompression rate. This positive correlation was later used by Toramaru (2006) to calibrate a model to predict the decompression rate of an eruption from the N_B of eruptive products. Our in-situ observations are consistent with previous experimental work and confirm this positive correlation between decompression rate and N_B. In fact, in the rapidly decompressed experiment (400 bar/min), the higher nucleation rate resulted in the formation of a larger number of smaller bubbles and the expansion of bigger ones, which produced a more heterogeneous BSD (Figure 6).

It is worth noting that bubble nucleation rate dropped to zero already at 100 bar below the initial pressure. A qualitatively similar effect was already observed by Mourtada-Bonnefoi and Laporte (2004). Nucleation of new bubbles always occurred in the largest portions of melt left empty by the resorption of smaller bubbles during the compression to 800 bar and generally at half distance between two near bubbles. This implies that the initial distribution of bubbles influences the rate of nucleation and, in general, when nucleation starts from an initial mono- or poly-disperse condition, it is expected to terminate when a critical N_B is achieved. This limit is given by the average distance between nearest bubbles, which should be larger than the mean diffusion distance (x), in order to allow the nucleation of new bubbles. The mean diffusion distance may be determined from the mean square distance of the two-dimensional diffusion equation:

$$x^2 = 2Dt$$

where D is the diffusion coefficient and t is time. Assuming a diffusion coefficient of water in the haplogranite of about 10^{-13} m^2/s (Nowak and Behrens, 1997), the mean diffusion distance is about 25 μm at 30 s and 50 μm at 120 s (i.e., the duration of a 100 bar decompression at rates of 50 and 200 bar/min, respectively). In this range of time, the diffusion path is comparable to the average distance between two nearest bubbles before decompression (30 μm), meaning that nucleation can initiate shortly after decompression, while stopping in favor of diffusive bubble growth after the reduction of the average bubble distance. In the case of the fastest decompression (400 bar/min), the diffusion path is much shorter than the average bubble distance and more bubbles nucleate, as visible from the flattening and left-shifting of the BSD (Figure 6b).

The limit of nucleation may not apply to degassing magmas, where the removal of bubbles creates more space in the melt for further nucleation. At a given temperature, the nucleation rate is therefore expected to be higher in melts characterized by lower viscosity (such as basalt and andesite), where degassing is promoted by the fast bubble coalescence and migration (Masotta et al., 2014). Conversely, degassing of a rhyolite is limited by the viscous resistance of the melt, which makes the time scale of coalescence longer than that of decompression, so that bubble preferentially evolve towards a close-packed state, inhibiting further nucleation. This is confirmed by the lack of coalescence during both pressure cycles and decompression paths applied to the haplogranitic melt, where bubbles pack closely while maintaining the same N_B.

Rapid decompression is thought to be the cause of explosive vesiculation, as it increases the volatile supersaturation, which builds up gas overpressure and causes magma fragmentation once this pressure exceeds the strength of melt walls between bubbles (Sparks et al. 1994; Mader et al. 1994; Alidibirov and Dingwell 1996; Mungall et al., 1996; Zhang, 1999; Martel et al. 2000). The

401 decompression at 400 bar/min is supposed to produce a higher volatile supersaturation than the
402 decompression at 50 bar/min, which should result in an earlier fragmentation. However, all
403 decompression paths produced similar textures until just before the fragmentation at about 200 bar,
404 meaning that (at least at the experimental conditions) the rate at which decompression occurs has
405 only minor effect on the final texture and fragmentation threshold. This suggests that the
406 fragmentation threshold must be controlled by the time scale of bubble coalescence, which
407 ultimately controls the permeable gas flow in the melt (outgassing). As discussed above,
408 decompression did not favor bubble coalescence at any of the rates used in the experiment, so that
409 permeable gas flow never developed and the final texture was controlled exclusively by the gas
410 bubble expansion, which acted in much shorter time scale.
411
412 **Consequences for natural systems**
413 From the observation of the effects of pressure cycling and decompression paths performed on the
414 haplogranite, and the comparison with previous in situ experiments with moissanite cell (Masotta et
415 al., 2014), general implications can be drawn. A major observation is that the time scale for bubble
416 coalescence increases dramatically in the more silicic melts, being maximum in the haplogranite,
417 where coalescence is not favored even when contact between bubbles is induced by the
418 decompression. Conversely, the time scale for coalescence in basalt and andesite is comparable or
419 even shorter than any pressure variation simulated in our experiments. The difference in time scales
420 among melts having different composition can be related to the interplay between diffusive growth
421 and viscous expansion, which is expressed by the Peclet number as the ratio of their time scales
422 (Lyakhovsky et al., 1996):
423

$$Pe = \frac{t_{dif}}{t_{vis}} = \frac{R^2 \Delta P}{D\eta}$$

424
425 where R is a typical bubble radius, D is the volatile diffusion coefficient and η is the viscosity of the
426 melt. Assuming average values for R (~10^{-5} m), D (~10^{-13} m^2/s) and η (~10^6 Pa·s), and considering
427 that ΔP is not less than 10^5 Pa, the Peclet numbers calculated for all these melts are larger than
428 unity, meaning that bubble growth is essentially controlled by time scale of diffusion. This explains
429 the faster coalescence observed in basalt and andesite, as due to the higher volatile diffusivities
430 compared to the rhyodacite and haplogranite. Upon decompression of these melts (i.e., during
431 magma ascent), the coalescence process may be strongly enhanced and the BSD is expected to
432 evolve towards even more heterogeneous distributions than those observed at isobaric conditions,
433 due to the combined effect of shear deformation and bubble channeling at the conduit wall (Bouvet
434 de Maisonneuve et al., 2009) and new nucleation in the bubble-free portions of melts. In addition,
435 the increased efficiency of coalescence during magma ascent increases magma permeability and,
436 consequently, reduces the time scale of magma fragmentation by favoring the permeable gas flow
437 (Koyaguchi et al., 2008; Richard et al., 2013). This is not the case of the haplogranite that, in
438 contrast, shows a relatively high porosity (up to 75% at pressure of 200 bar) in spite of an evidently
439 low connected porosity. Notably, the same condition of bubble packing was achieved in all
440 decompression paths at the same pressure of 200 bar. This value can be compared with the
441 fragmentation threshold, defined by Scheu et al. (2006) as the pressure at which fragmentation
442 occurs upon decompression. According to the model of Koyaguchi et al. (2008), the fragmentation

threshold increases with decreasing connected porosity of the sample and reaches 200 bar when connected porosity is lower than 10%, a condition that matches the experimental case.

Implications

The new hydrothermal moissanite cell allows to observe in-situ bubble nucleation and growth under precisely controlled pressure conditions. The cell represents an implementation of the original moissanite cell presented in Schiavi et al. (2010), redesigned to perform experiments at temperature up to 850 °C and pressure up to 2000 bar, at controlled T-P-t paths. Preliminary experiments were performed using a haplogranite starting glass and simulating pressure oscillations that can occur in shallow magma chambers due to changes of eruption rates (Huppert and Woods, 2002) or in volcanic conduits as response to pressure variations generated during the expansion and bursting of gas slugs ascending in conduits (James et al., 2004; Del Bello et al., 2012). Decompression was studied at constant rates typical of vulcanian to plinian eruptions (Miwa and Geshi, 2012).
For the haplogranitic melt, faster rates of decompression promote bubble nucleation, because of the shorter mean diffusion distance. In non-degassing systems, nucleation terminates when this distance is shorter than the average distance between two close bubbles. Coalescence is not favored by the contact between bubbles induced during the pressure cycles and decompressions, meaning that the time scale for melt-film drainage is longer than the longest time of interaction between two bubbles (i.e. >60 s). On the other hand, Ostwald ripening seems to be favored by the pressure cycles, due to the difference in time scale between volatile diffusion and bubble volume change. Upon decompression at constant rate, the melt reaches a fragmentation threshold at about 200 bar, independent of the decompression rate applied. Further experiments with the new hydrothermal moissanite cell will allow a better quantification of the time scales of bubble nucleation, growth and melt fragmentation, as well as the of the effects of the initial state of the melt on these processes.

Acknowledgements

We are grateful to Hubert Schulze for sample preparation, to Sven Linhardt and Kurt Klasinski for constructing the spindle drive and its control system, and to Svyatoslav Shcheka for assistance during experiment and BSE image collection. Constructive reviews by two referees improved this manuscript. This work was supported by Humboldt fellowship to MM.

References cited

Alidibirov, M. and Dingwell, D.B. (1996) Magma fragmentation by rapid decompression. Nature, 380, 146–148.

Bagdassarov, N., Dorfman, A., and Dingwell, D.B. (2000) Effect of alkalis, phosphorus, and water on the surface tension of haplogranite melt. American Mineralogist, 85, 33–40.

Bouvet de Maisonneuve., C., Bachmann, O., and Burgisser, A. (2009) Characterization of juvenile pyroclasts from the Kos Plateau Tuff (Aegean Arc): insights into the eruptive dynamics of a large rhyolitic eruption. Bulletin of Volcanology, 71, 643–658.

Chen, M.K., and Voorhees, P.W. (1993) The dynamics of transient Ostwald ripening. Modelling and Simulation in Materials Science and Engineering 1(5), 591–612.

Del Bello, E., Llewellin, E.W., Taddeucci, J., Scarlato, P., and Lane S.J. (2012) An analytical model for gas overpressure in slug-driven explosions: Insights into Strombolian volcanic eruptions. Journal of Geophysical Research Solid Earth, 117, B02206.

Fiege, A., and Cichy, S.B (2015) Experimental constraints on bubble formation and growth during magma ascent: A review. American Mineralogist, 100, 2426-2442.

Gardner, J.E., Hilton, M., and Carroll, M.R. (1999) Experimental constraints on degassing of magma: isothermal bubble growth during continuous decompression from high pressure. Earth and Planetary Science Letters, 168, 201-218.

Gardner, J.E. (2007) Heterogeneous bubble nucleation in highly viscous silicate melts during instantaneous decompression from high pressure. Chemical Geology, 236, 1–12.

Gardner, J.E., and Ketcham, R.A. (2011) Bubble nucleation in rhyolite and dacite melts: temperature dependence of surface tension. Contributions to Mineralogy and Petrology, 162, 929–943.

Gondé, C., Massare, D., Bureau, H., Martel, C., Pichavant, M., and Clocchiatti, R. (2006) In situ study of magmatic processes: a new experimental approach. High Pressure Research, 26, 243–250.

Gondé, C., Martel, C., Pichavant, M., and Bureau, H. (2011) In situ bubble vesiculation in silicic magmas. American Mineralogist, 96, 111–124.

Hess, K-U., and Dingwell, D.B. (1996) Viscosities of hydrous leucogranitic melts: A non-Arrhenian model. American Mineralogist, 81, 1297–1300.

Holtz, F., Behrens, H., Dingwell, D.B., and Johannes, W. (1995) Water solubility in haplogranitic melts. Compositional, pressure and temperature dependence. American Mineralogist, 80, 94-108.

Huppert, H.E., and Woods, A.W. (2002) The role of volatiles in magma chamber dynamics. Nature, 420, 493-495.

James, M.R., Lane, S.J. and Chouet, B. (2004) Pressure changes associated with the ascent and bursting of gas slugs in liquid-filled vertical and inclined conduits. Journal of Volcanology and Geothermal Research, 129 (1-3), 61-82.

Koyaguchi, T., Scheu, B Mitani, N.K., and Melnik, O. (2008) A fragmentation criterion for highly viscous bubbly magmas estimated from shock tube experiments. Journal of Volcanology and Geothermal Research, 178, 58-71.

Lautze, N., Sisson, T., Mangan, M., and Grove, T. (2011) Segregating gas from melt: an experimental study of the Ostwald ripening of vapor bubbles in magmas. Contributions to Mineralogy and Petrology, 161, 331–347.

Lensky, N.G., Navon, O., and Lyakhovsky, V. (2004) Bubble growth during decompression of magma: Experimental and theoretical investigation. Journal of Volcanology and Geothermal Research, 129, 7–22.

Lyakhovsky, V., Hurwitz, S., and Navon, O. (1996) Bubble growth in rhyolitic melts: experimental and numerical investigation. Bulletin of volcanology, 58, 19–32.

Mader, H.M., Zhang, Y., Phillips, J.C., Sparks, R.S.J., Sturtevant, B., and Stolper, E. (1994) Experimental simulations of explosive degassing of magma. Nature, 372, 85–88.

Mangan, M., and Sisson, T. (2000) Delayed, disequilibrium degassing in rhyolite magma: decompression experiments and implications for explosive volcanism. Earth and Planetary Science Letters, 183, 441–455.

Martel, C., Dingwell, D.B., Spieler, O., Pichavant, M. and Wilke, M. (2000) Fragmentation of foamed silicic melts: an experimental study. Earth and Planetary Science Letters, 178, 47–58.

Martel, C., and Bureau, H. (2001) In situ high-pressure and high-temperature bubble growth in silicic melts. Earth and Planetary Science Letters, 191, 115–127.

Masotta, M., Ni, H., and Keppler, H. (2014) In situ observations of bubble growth in basaltic, andesitic and rhyodacitic melts. Contributions to Mineralogy and Petrology, 167, 967.

Masotta, M., and Keppler, H. (2015) Anhydrite solubility in differentiated arc magmas. Geochimica et Cosmochimica Acta, 158, 79–102.

Miwa, T., and Geshi, N. (2012) Decompression rate of magma at fragmentation: Inference from broken crystals in pumice of vulcanian eruption. Journal of Volcanology and Geothermal Research, 227, 76-84.

Mourtada-Bonnefoi, C.C., and Laporte, D. (1999) Experimental study of homogeneous bubble nucleation in rhyolitic magmas. Geophysical Research Letters, 26, 3505–3508.

Mourtada-Bonnefoi, C.C., Laporte, D. (2002) Homogeneous bubble nucleation in rhyolitic magmas: an experimental study of the effect of H_2O and CO_2. Journal of Geophysical Research, 107, B4.

Mourtada-Bonnefoi, C.C., and Laporte, D. (2004) Kinetics of bubble nucleation in a rhyolitic melt: an experimental study of the effect of ascent rate. Earth and Planetary Science Letters, 218, 521–537.

Mungall, J.E., Bagdassarov, N.S., Romano, C., and Dingwell, D.B. (1996) Numerical modelling of stress generation and microfracturing of vesicle walls in glassy rocks. Journal of Volcanology and Geothermal Research, 73, 33-46.

Ni, H., Keppler, H., Walte, N., Schiavi, F., Chen, Y., Masotta, M., and Li, Z. (2014) In situ observation of crystal growth in a basalt melt and the development of crystal size distribution in igneous rocks. Contributions to Mineralogy and Petrology, 167 (5), 1–13.

Nowak, M., Behrens, H. (1997) An experimental investigation on diffusion of water in haplogranitic melts. Contributions to Mineralogy and Petrology 126, 365–376.

Preuss, O., Marxer, H., Ulmer, S., Wolf, J., and Nowak, M. (2016) Degassing of hydrous trachytic Campi Flegrei and phonolitic Vesuvius melts: Experimental limitations and chances to study homogeneous bubble nucleation. American Mineralogist, 101, 859-875.

Richard, D., Scheu, B., Mueller, S.P., Spieler, O., and Dingwell D.B. (2013) Outgassing: Influence on speed of magma fragmentation. Journal of Geophysical Research Solid Earth, 118, 862–877.

Ryan, A.G., Russell, J.K., Hess, K.-U., Phillion, A.B., and Dingwell D.B. (2015) Vesiculation in rhyolite at low H_2O contents: A thermodynamic model. Geochemistry, Geophysics, Geosystems, 16, 4292– 4310.

Schiavi, F., Walte, N., Konschak, A., Keppler, H. (2010) A moissanite cell apparatus for optical in situ observation of crystallizing melts at high temperature. American Mineralogist, 95, 1069-1079.

Scheu, B., Spieler, O., and Dingwell, D.B. (2006) Dynamics of explosive volcanism at Unzen volcano: an experimental contribution. Bulletin of Volcanology 69 (2), 175–187.

Sparks, R.S.J., Barclay, J., Jaupart, C., Mader, H.M., and Phillips, J.C. (1994) Physical Aspects of Magma Degassing I. Experimental and theoretical constraints on vesiculation. Reviews in Mineralogy, 30, 413–445.

Toramaru, A. (2006) BND (bubble number density) decompression rate meter for explosive volcanic eruptions. Journal of Volcanology and Geothermal Research, 154, 303–316.

Withers, A.C., and Behrens, H. (1999) Temperature-induced changes in the NIR spectra of hydrous albitic and rhyolitic glasses between 300 and 100 K. Physics and Chemistry of Minerals, 27, 119-132.

Yamada, K., Emori, H., and Nakazawa, K. (2008) Time-evolution of bubble formation in a viscous liquid. Earth Planets Space, 60(6), 661–679.

Zhang Y (1999) A criterion for the fragmentation of bubbly magma based on brittle failure theory. Nature, 402, 648–650.

Figures Caption

Figure 1. Construction scheme (**a**) and pictures (**b**) of the new hydrothermal moissanite cell before and during an experiment.

Figure 2. P-t path of the experiment HGT-2 showing (**a**) the two cycles and the three decompression paths, and (**b**) magnification of the two pressure cycles showing the different periods.

585 **Figure 3.** Sequence of images of showing bubble nucleation and growth under isobaric conditions. Ostwald
586 ripening occurs in the isobaric stage following pressure perturbations, as indicated by red arrows.
587 **Figure 4.** Variation of bubble number density, N_B (**a**), bubble size distribution, BSD (**b**), and cumulative
588 BSD (c) over time at isobaric conditions (P = 600 bar).
589 **Figure 5**. Images collected at different pressures (700, 600 and 500 bar) and different cycles (1, 4 and 7)
590 during the 120 s period cycling. The red arrow shows two adjacent bubbles, which fully coalesce during a
591 single cycle.
592 **Figure 6.** Comparison between images (**a**) and BSD (**b**) collected at 700 and 600 bar, during the three
593 decompression paths of 50 bar/min (left), 200 bar/min (center), and 400 bar/min (right). The rectangles
594 indicate portion of melts (at half distance between close bubbles) were most of the nucleation occurred
595 during the first 100 bar decompression.
596 **Figure 7.** Backscattered electron images showing the texture of two experimental samples: (**a**) sample
597 decompressed until fragmentation at 200 bar and (**b**) non-fragmented sample cooled to room temperature
598 with a rate of 30 °C/min at isobaric conditions, after decompression to 400 bar. Note that small feldspar
599 crystals formed in the melt during the slow cooling.

This is a preprint, the final version is subject to change, of the American Mineralogist (MSA)
Cite as Authors (Year) Title. American Mineralogist, in press.
(DOI will not work until issue is live.) DOI: http://dx.doi.org/10.2138/am-2017-6093

Figure 1

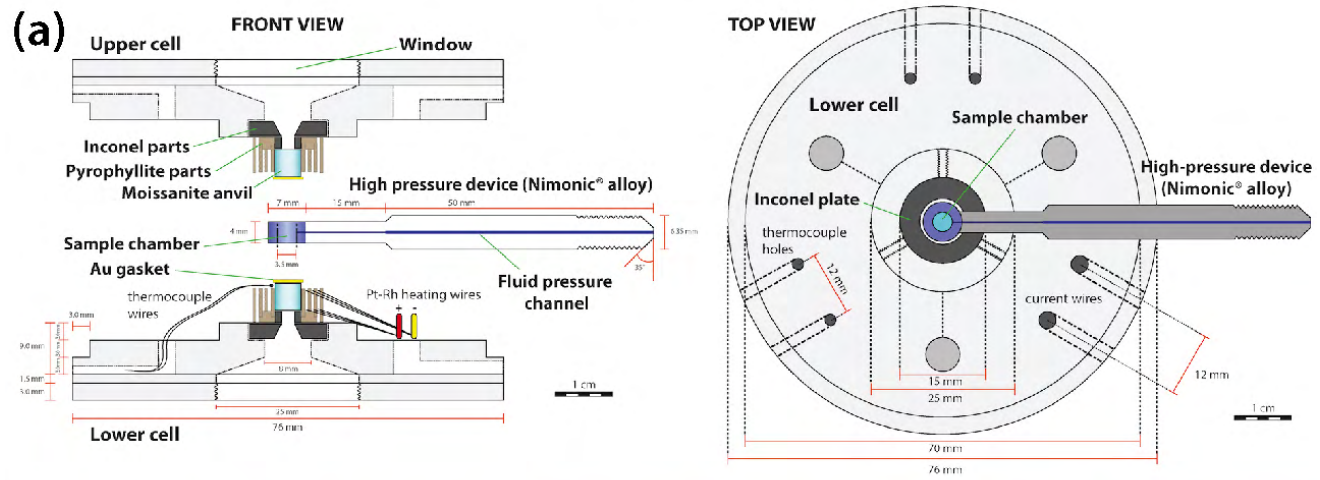

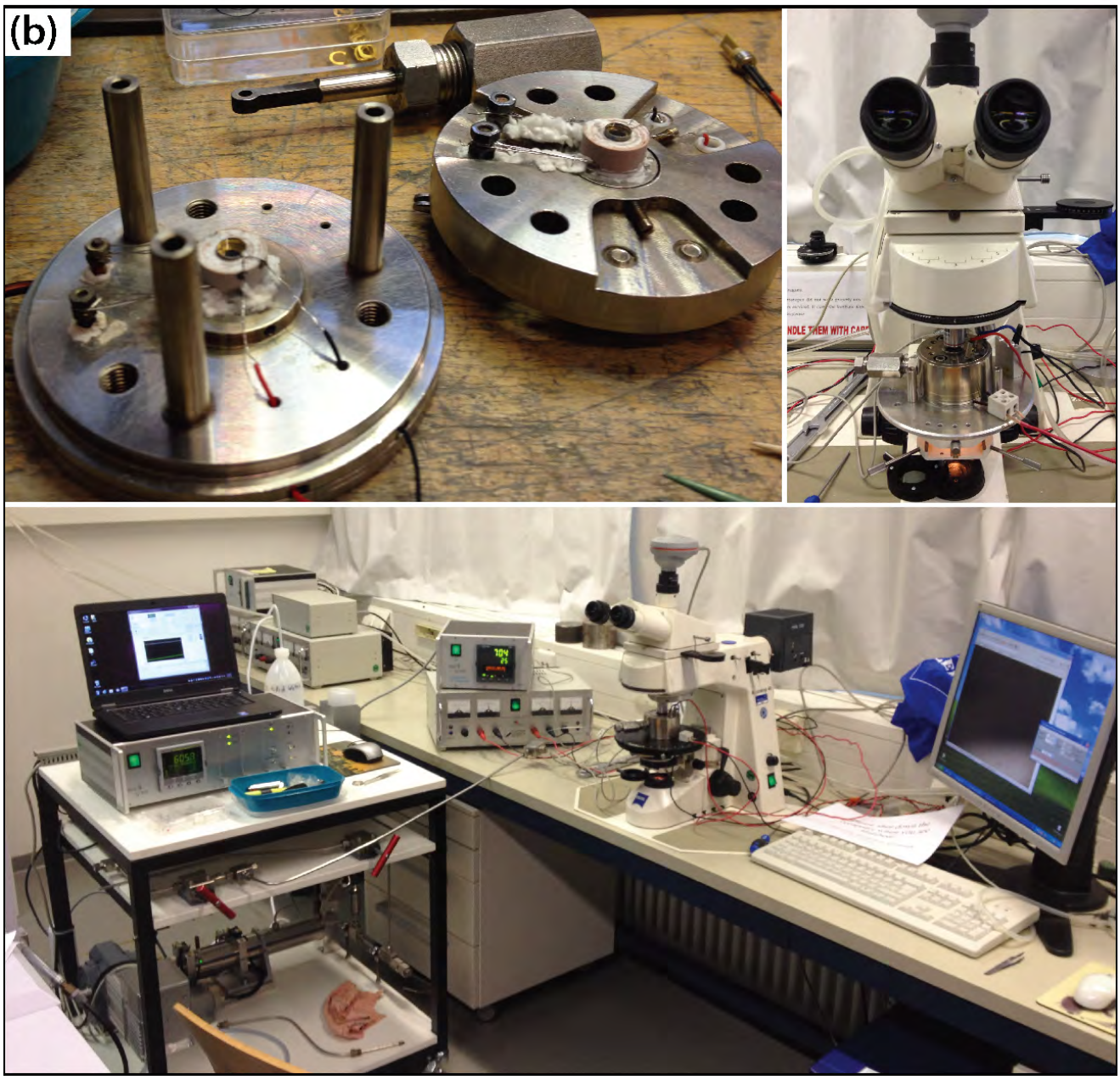

This is a preprint, the final version is subject to change, of the American Mineralogist (MSA)
Cite as Authors (Year) Title. American Mineralogist, in press.
(DOI will not work until issue is live.) DOI: http://dx.doi.org/10.2138/am-2017-6093

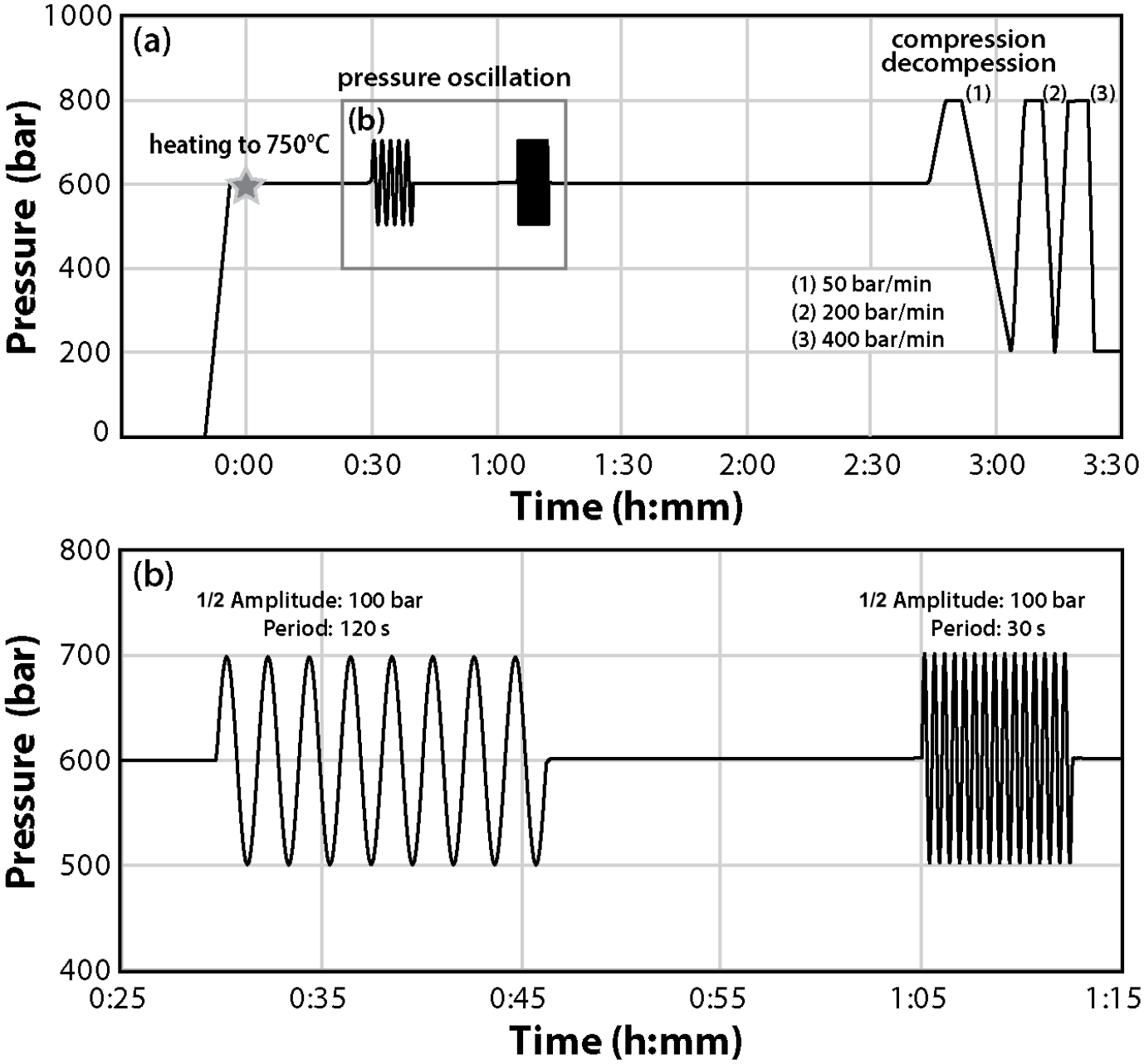

This is a preprint, the final version is subject to change, of the American Mineralogist (MSA)
Cite as Authors (Year) Title. American Mineralogist, in press.
(DOI will not work until issue is live.) DOI: http://dx.doi.org/10.2138/am-2017-6093

Figure 3

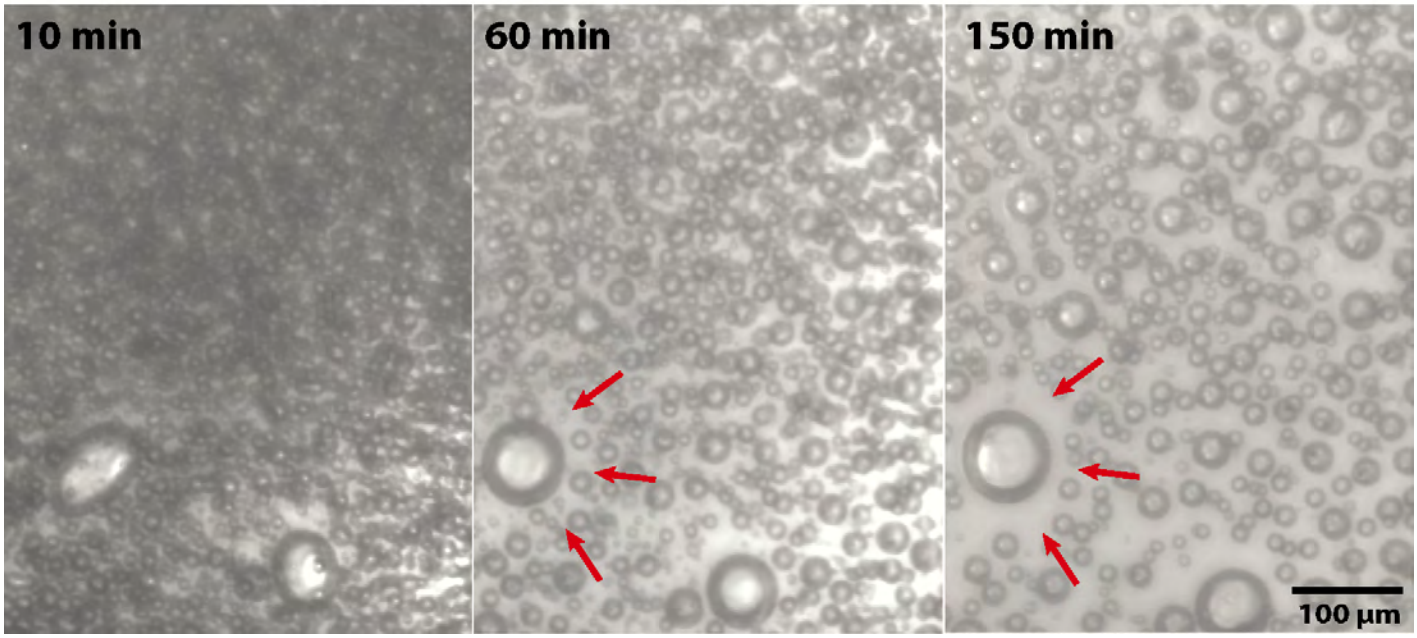

This is a preprint, the final version is subject to change, of the American Mineralogist (MSA)
Cite as Authors (Year) Title. American Mineralogist, in press.
(DOI will not work until issue is live.) DOI: http://dx.doi.org/10.2138/am-2017-6093

Figure 4

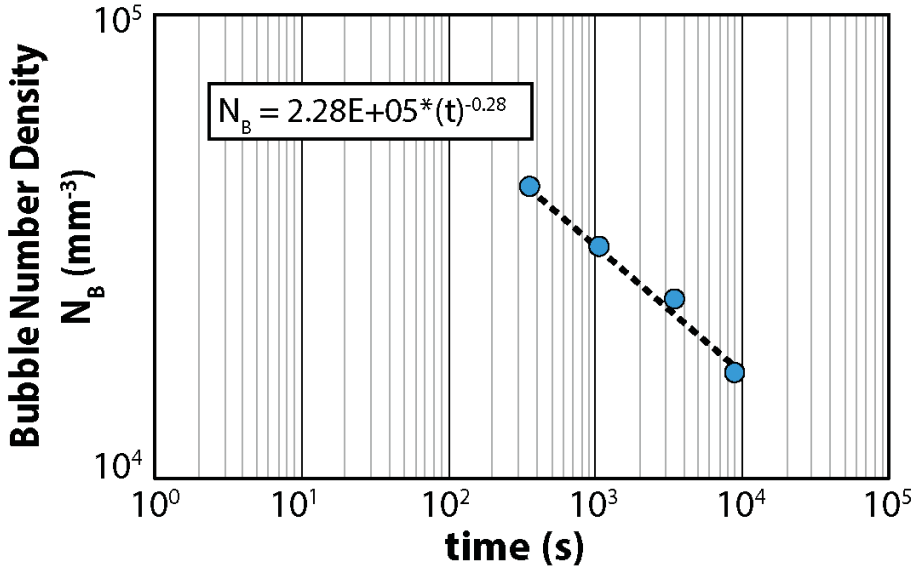

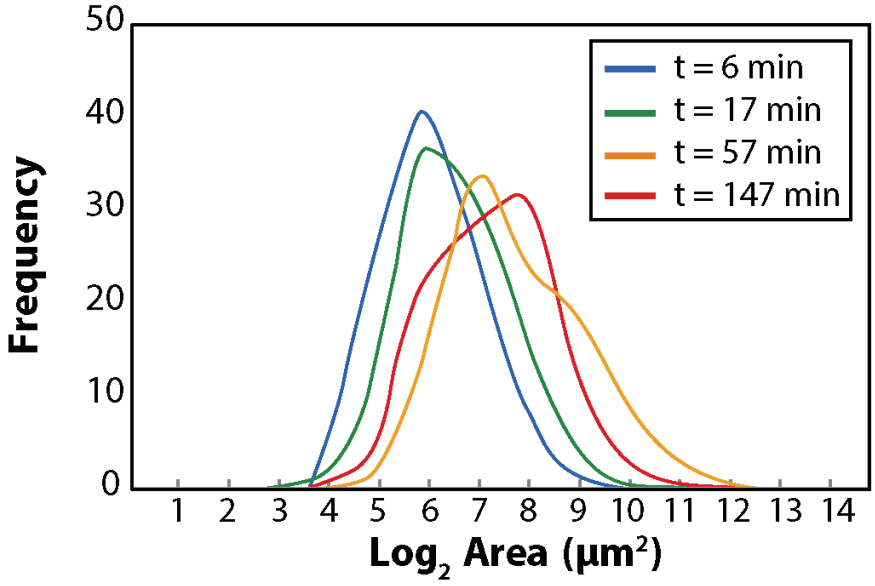

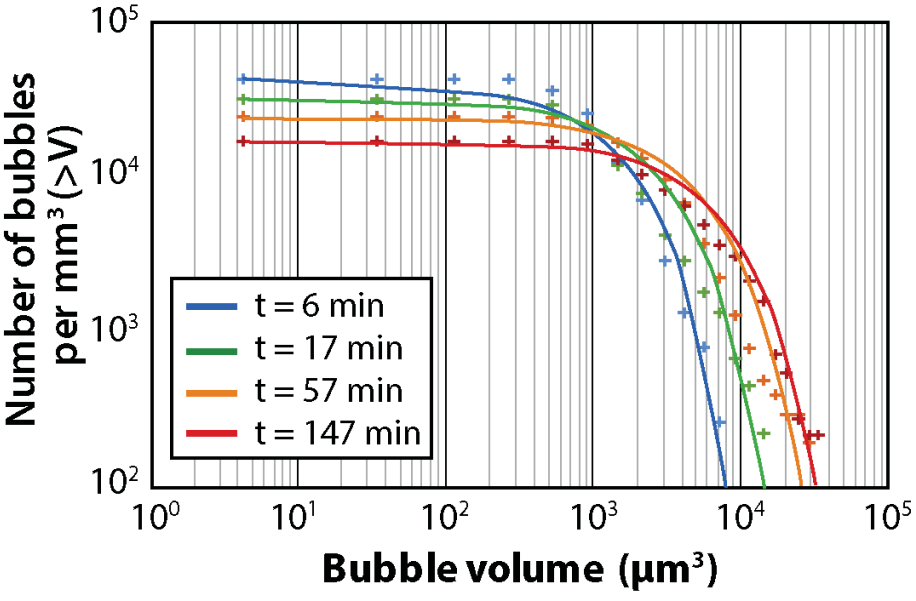

This is a preprint, the final version is subject to change, of the American Mineralogist (MSA)
Cite as Authors (Year) Title. American Mineralogist, in press.
(DOI will not work until issue is live.) DOI: http://dx.doi.org/10.2138/am-2017-6093

Figure 5

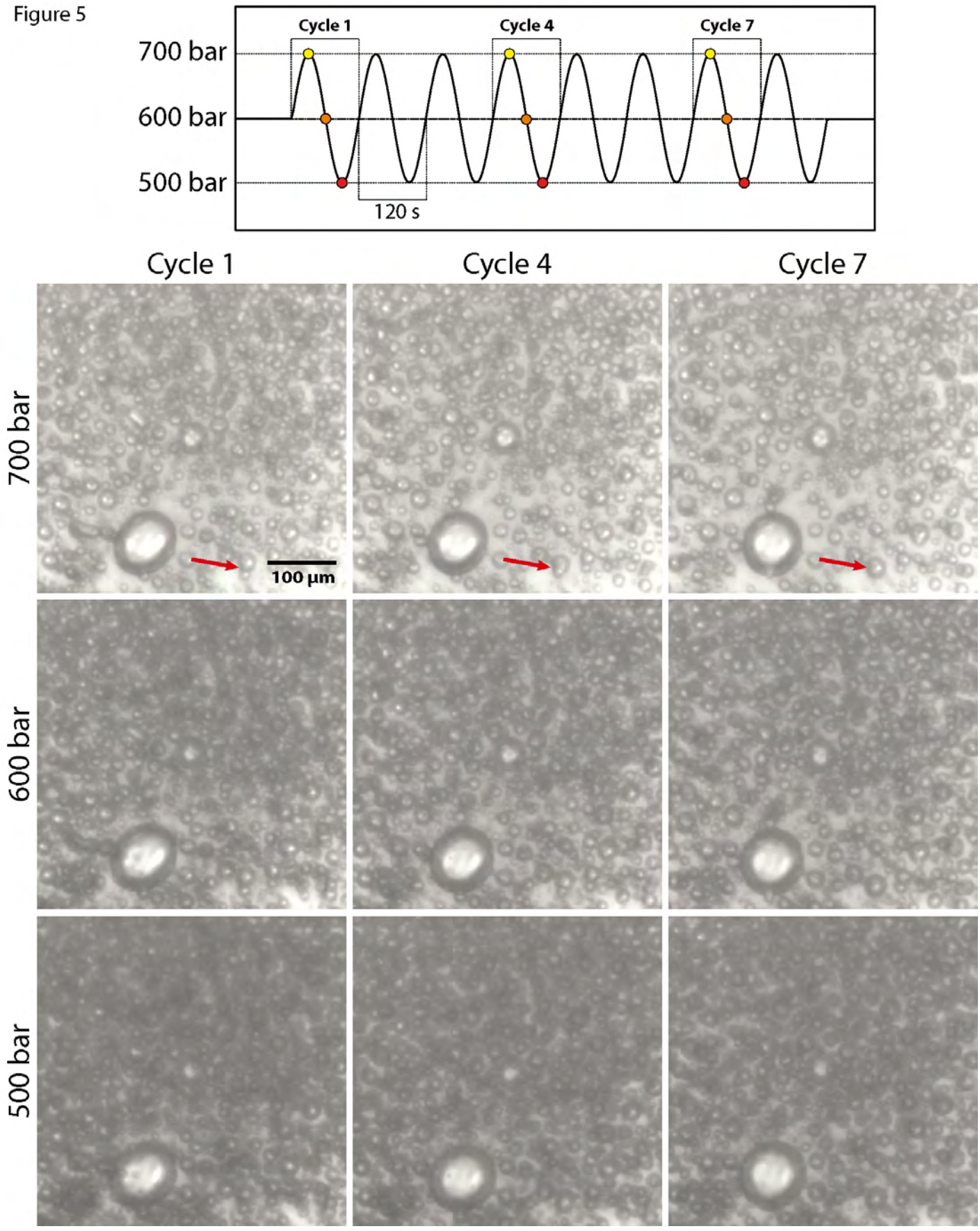

This is a preprint, the final version is subject to change, of the American Mineralogist (MSA)
Cite as Authors (Year) Title. American Mineralogist, in press.
(DOI will not work until issue is live.) DOI: http://dx.doi.org/10.2138/am-2017-6093

Figure 8

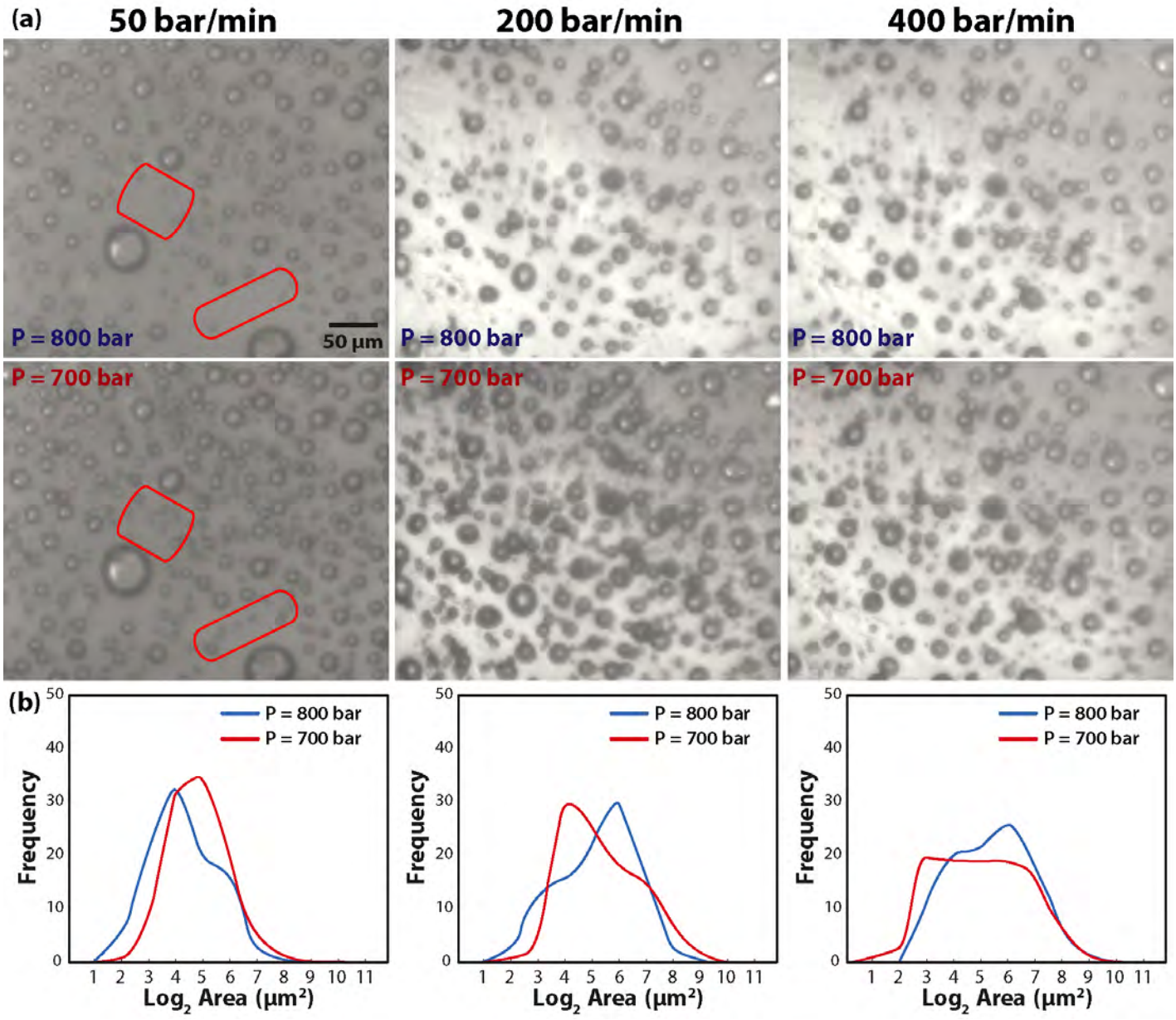

This is a preprint, the final version is subject to change, of the American Mineralogist (MSA)
Cite as Authors (Year) Title. American Mineralogist, in press.
(DOI will not work until issue is live.) DOI: http://dx.doi.org/10.2138/am-2017-6093

Figure 7

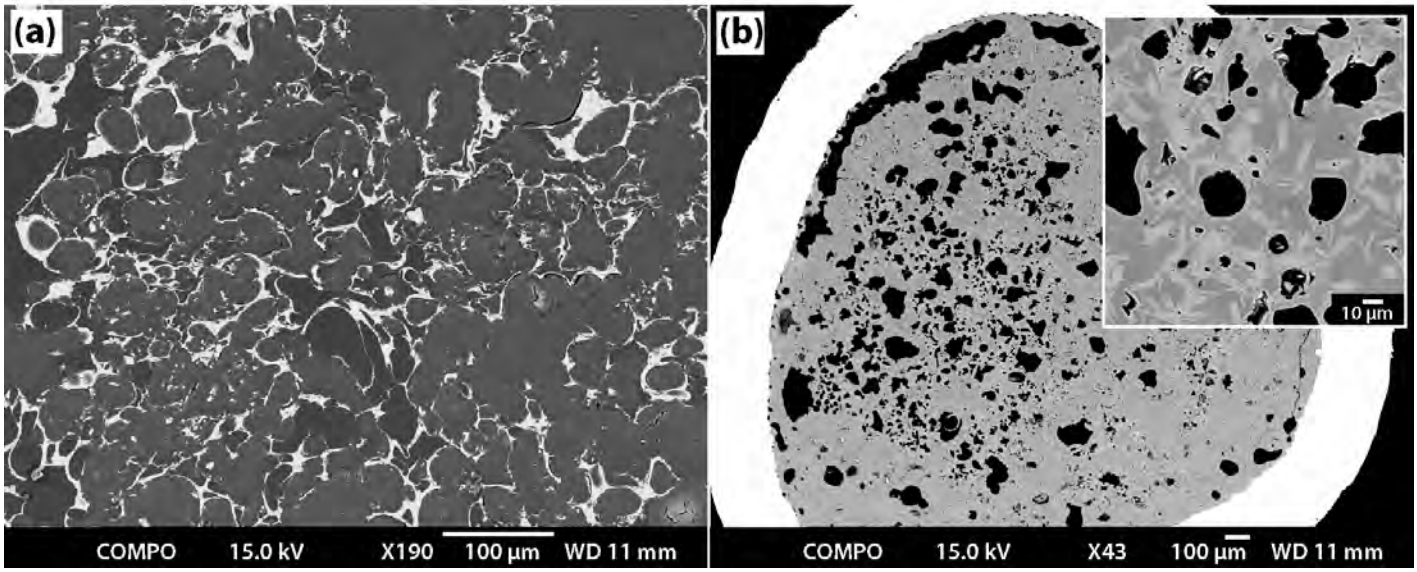

This is a preprint, the final version is subject to change, of the American Mineralogist (MSA)
Cite as Authors (Year) Title. American Mineralogist, in press.
(DOI will not work until issue is live.) DOI: http://dx.doi.org/10.2138/am-2017-6093

Table 1. Details of experiments investigating the effect of pressure oscillations on vapor bubbles in haplogranitic melt.

Exp.	T (°C)	P_{mean} (bar)	½ *f* (bar)	Period (s)	Observations
HGT-1	715	500	50	20	no change of N_B
		500	50	40	no change of N_B
		500	100	60	small change of N_B
		500	200	10	moderate change of N_B
		500	200	20	moderate change of N_B
HGT-2	715	600	100	120	small change of N_B
		600	100	30	small change of N_B
HGT-3	715	600	100	60	small change of N_B
		600	100	15	small change of N_B
		600	100	8	small change of N_B
		600	200	40	moderate change of N_B
		600	400	20	large change of N_B

Symbol legend. P_{mean}: average (static) pressure, ½ *f*: half amplitude of pressure oscillations, N_B: bubble number density

This is a preprint, the final version is subject to change, of the American Mineralogist (MSA)
Cite as Authors (Year) Title. American Mineralogist, in press.
(DOI will not work until issue is live.) DOI: http://dx.doi.org/10.2138/am-2017-6093

Table 2. Details of decompression experiments

Exp.	T (°C)	$P_{init.}$ (bar)	P_{final} (bar)	Rate (bar/min)	Observations
HGT-1	715	800	400	300	no fragmentation
HGT-2	715	800	200	50	no fragmentation after 1s at 200 bar
		800	200	200	no fragmentation after 1s at 200 bar
		800	200	400	fragmentation after 5s at 200 bar
HGT-3	715	800	300	100	no fragmentation
		800	300	300	no fragmentation

Symbol legend. P_{init}: initial pressure before decompression, P_{final}: final pressure after decompression

This is a preprint, the final version is subject to change, of the American Mineralogist (MSA)
Cite as Authors (Year) Title. American Mineralogist, in press.
(DOI will not work until issue is live.) DOI: http://dx.doi.org/10.2138/am-2017-6093

Table 3. Results from image analyses of experiment HGT-2, carried out at different experimental times.

t (min)	P (bar)	ϕ	r (μm)	G_R (mm/s)	N_B (mm^{-3})	Note
6	600	0.33	5.6 - 8.0	$5(\pm1)\cdot10^{-6}$	$4.29\cdot10^{4}$	isobaric P = 600 bar
17	600	0.34	6.9 - 9.8	$2(\pm1)\cdot10^{-7}$	$3.18\cdot10^{4}$	isobaric P = 600 bar
57	600	0.40	10.0 - 13.1	$2(\pm1)\cdot10^{-7}$	$2.43\cdot10^{4}$	isobaric, after cycle 100 bar/120 s
147	600	0.37	10.3 - 15.1	$2(\pm1)\cdot10^{-7}$	$1.69\cdot10^{4}$	isobaric, after cycle 100 bar/30 s
185	400	0.45	6 - 30	$2(\pm1)\cdot10^{-5}$	$2.40\cdot10^{4}$	during decompression at 50 bar/min
208	400	0.50	4 - 20	$1(\pm0.5)\cdot10^{-4}$	$3.16\cdot10^{4}$	during decompression at 400 bar/min

Symbol legend. ϕ: vesicularity, r: average range of bubble radius, G_R: growth rate, N_B: bubble number density. G_R measured during the decompression paths are calculated from the beginning of decompression.